Large Seasonal Modulation of Tides due to Ice Cover Friction in a Midlatitude Estuary*

NICKITAS GEORGAS

Stevens Institute of Technology, Hoboken, New Jersey

(Manuscript received 27 March 2011, in final form 2 July 2011)

ABSTRACT

Seasonal episodes of significant tidal damping (reductions of tidal amplitudes as much as 50%) and tidal modulation were observed in the Hudson River estuary in the course of three consecutive winters from multiple tide gages. Through comparisons with United States Coast Guard ice reports, it was hypothesized that these events correspond with an increase in ice concentration and the development of a seasonal ice field within the upper 170 km of the tidal Hudson north of Peekskill, New York. Using stationary (tidal harmonic) and nonstationary (wavelet) analyses as well as numerical modeling, it is shown that under-ice friction is the primary cause of the observed modulations in tidal circulation (water levels and currents) throughout the 240-km-long estuary. Upstream of the ice field edge at Peekskill, depth-averaged tidal currents are greatly reduced under the ice cover through first-order damping, and vertical current profiles under the ice become parabolic. Tidal ranges increase near the edge of the ice field, and, south of that, on Manhattan's western shores, currents increase because of tidal wave reflection. These amplified currents create stronger vertical mixing leading to a less stratified estuary and decreasing salt front intrusion. At the other end, near Troy, tidal flows become smaller relative to the river's streamflow, leading to increased ebb predominance and ebb-directed flows down to the port of Albany. Also, the increased friction leads to a higher sea level setup there. During such episodes, astronomical tide–based and operational forecast model predictions that neglected ice are severely compromised.

1. Introduction

The effect of ice on hydrodynamics has been observed and studied in nontidal rivers and streams (e.g., USGS 1982; USACE 2006; WMO 2010) and in lakes and reservoirs (e.g., USACE 1997; Bengtsson 1996; Maln et al. 1998; Wang et al. 2010; Hutula et al. 2010), including subglacial lakes (Thoma et al. 2010; Sergienko and Hulbe 2011). In wide and/or midlatitude rivers, the ice cover is in floatation (USGS 1982) because the air is not sufficiently frigid to allow for fusion of the ice cover to the channel banks (USACE 2006). Instead, streamwise tension cracks form along the banks that appear and refreeze in dynamic equilibrium (USGS 1982; WMO 2010). Thus, the ice cover is free to float vertically, but with hindered or stalled horizontal motion. The formation of an ice cover on a river increases frictional resistance, because a water–ice interface replaces the water–air interface, and roughly doubles the wetted perimeter of a wide channel, and the cross-sectional area decreases depending on ice draft (USGS 1982; USACE 2006). According to USACE (2006), ''the added resistance in flow, along with the reduction in flow area caused by the ice, results in higher stages than a comparable open-water discharge would produce.'' Thus, streamflow rating curves (stage–discharge relationships) are notoriously unreliable during ice cover periods in nontidal rivers and reservoirs (USGS 1982; WMO 2010; USACE 1997). Tidal flows add another significant complication.

Previous studies of ice effects on tidal hydrodynamics

Sverdrup (1926) first discussed the effects of an ice cover on long gravity waves in the north Siberian shelf. Reduced phase speed, decreasing amplitude as the waves progress, and phase lag between maximum current and high water were found to result from the effect of friction (Sverdrup

* Supplemental information related to this paper is available at the Journals Online website at http://dx.doi.org/10.1175/JPO-D-11-063.s1.

Corresponding author address: Nickitas Georgas, Stevens Institute of Technology, 711 Hudson Street, Hoboken, NJ 07030.
E-mail: nickitas.georgas@stevens.edu

DOI: 10.1175/JPO-D-11-063.1

1926; Høydalsvik and Weber 2003). There is a substantial volume of research on the Arctic and Antarctic regions (e.g., MacAyeal 1984; Pease and Overland 1984; Godin 1986; Smithson et al. 1996; St-Laurent et al. 2008; Kagan and Sofina 2010; Nguyen et al. 2011, and references therein). Volkov et al. (2002) summarize 60 yr of research in the Kara Sea (Russian Arctic), where tidal amplitudes are known to decrease during winter and the onset of high tide is later than in the summer. Godin and Barber (1980), Godin (1986), and Prinsenberg (1988) used tidal admittance analyses to examine the seasonal variability of tides in and around the Hudson Bay system, Canada, which they hypothesized was due to ice cover either through changes in resonance and geomorphic constraints (Godin and Barber 1980) and/or through ice–water friction (Godin 1986; Prinsenberg 1986, 1988). More recently, Saucier et al. (2004) and St-Laurent et al. (2008) tested the frictional hypothesis with numerical models, proving that the observed M2 amplitude variations (importantly, both local decreases but also local increases) in the Hudson Bay system are due to under-ice friction.

There are relatively few studies that have focused on the effect of an ice cover on tides in an estuary or a tidal river (Morse et al. 1999, 2006a). In the macrotidal (11.7-m mean tidal range) environment of the Minas Basin–Cobequid Bay area, northeast Bay of Fundy, Canada (45°20′N), anchored ice walls are formed from stranded ice and sediment along the shore (Knight and Dalrymple 1976; Desplanque and Bray 1986), transforming the trapezoidal cross sections of tidal creeks into rectangular channels of smaller cross-sectional area, reducing the tidal prism (Desplanque and Mossman 1998).

In the study most relevant to the present work, Morse et al. (2006a) quantified the effects of a standing ice cover on the hydrodynamics of a relatively short, shallow, mesotidal estuary off the Gulf of St. Laurence in Quebec, Canada, the Portneuf. Based on a numerical model and field observations, the midwinter 50-cm-thick ice cover produced an attenuation of the neap tidal range (1.9 m) and spring tidal range (4.0 m) of 17% and 37%, respectively, near the upstream end of the estuary. The arrival of low water was also delayed by about 90 min at this location. In general, the ice cover attenuated peak velocities by 12%–20%, although at certain times and locations the ice cover could induce higher velocities than would be present under open water conditions. The ice cover also retarded and diminished the salt wedge intrusion (Morse et al. 2006a). No study of the effect of the seasonal ice cover on the tidal hydrodynamics of the Hudson River estuary (HRE) is known; in fact, no such study is known for any microtidal estuary outside the world's severe or moderately cold regions. It will be shown herein that ice–tide interaction is an important overlooked seasonal feature of tidal hydrodynamics in the HRE; its effects could potentially be observed in other similar midlatitude estuaries with seasonal ice cover.

2. Background

a. The Hudson River estuary

The HRE (Fig. 1) is one of the most studied and modeled estuaries in the world. The general tidal hydrodynamics of the HRE have been studied by many investigators in the past using in situ observations (e.g., Abood 1974; Jay and Bowman 1975; Swanson 1976; Geyer et al. 2000; Abood et al. 2006; Nitche et al. 2007) and numerical models (e.g., Blumberg et al. 1999; Warner et al. 2005; Miller and St John 2006; Blumberg and Hellweger 2006; Ralston et al. 2008; Haidvogel et al. 2008; Scully et al. 2009; Georgas and Blumberg 2010). Yet, most of these studies focused in the spring freshet and summer-fall periods, and none has mentioned tide–ice interaction during winter. To set the stage, a short summary of HRE hydrodynamics follows.

At its southern entrance at the southern tip of Manhattan Island at the Battery, the Hudson River is connected to the Atlantic Ocean (i) directly through the upper and lower New York/New Jersey Harbor and (ii) through Long Island Sound via a lower East River (secondary) and Harlem River (tertiary) connection (Fig. 1). The oceanic tide enters the HRE at the Battery and travels up to Troy, 243 km upstream, where the tidal wave is reflected by a dam. The lower HRE is partially mixed, with significant stratification variability based on the neap–spring cycle (Geyer et al. 2000). Salt intrudes from 30 to over 130 km upstream of the Battery, depending on river discharge and tidal forcing (e.g., Abood 1974). Upstream, near Troy, the major contributions to streamflow come from the Hudson over the Troy Dam, and its main tributary the Mohawk River at Cohoes, New York, with a combined long-term annual-mean flow of 250 $m^3 s^{-1}$. The long-term mean freshwater flow reaching the southern tip of Manhattan due to the Hudson, its tributaries, and other inflows is about 400 $m^3 s^{-1}$, though it can be over 3 times that in early spring or just 1/3 of that in late summer.

The tide at the Battery is semidiurnal with the following amplitudes: M2 = 66.6 cm, S2 = 13.1 cm, N2 = 15.0 cm, K2 = 3.5 cm, K1 = 10.2 cm, O1 = 5.1 cm, Q1 = 1.1 cm, M4 = 2.6 cm, and M6 = 2.4 cm. Around West Point and Poughkeepsie, the principal M2 amplitude drops to 45–46 cm. It increases again upstream, and at Albany, New York, the tide becomes mixed semidiurnal (form number 0.253) with the following amplitudes: M2 = 71.4 cm, S2 = 9.2 cm, N2 = 12.3 cm, K2 = 2.6 cm,

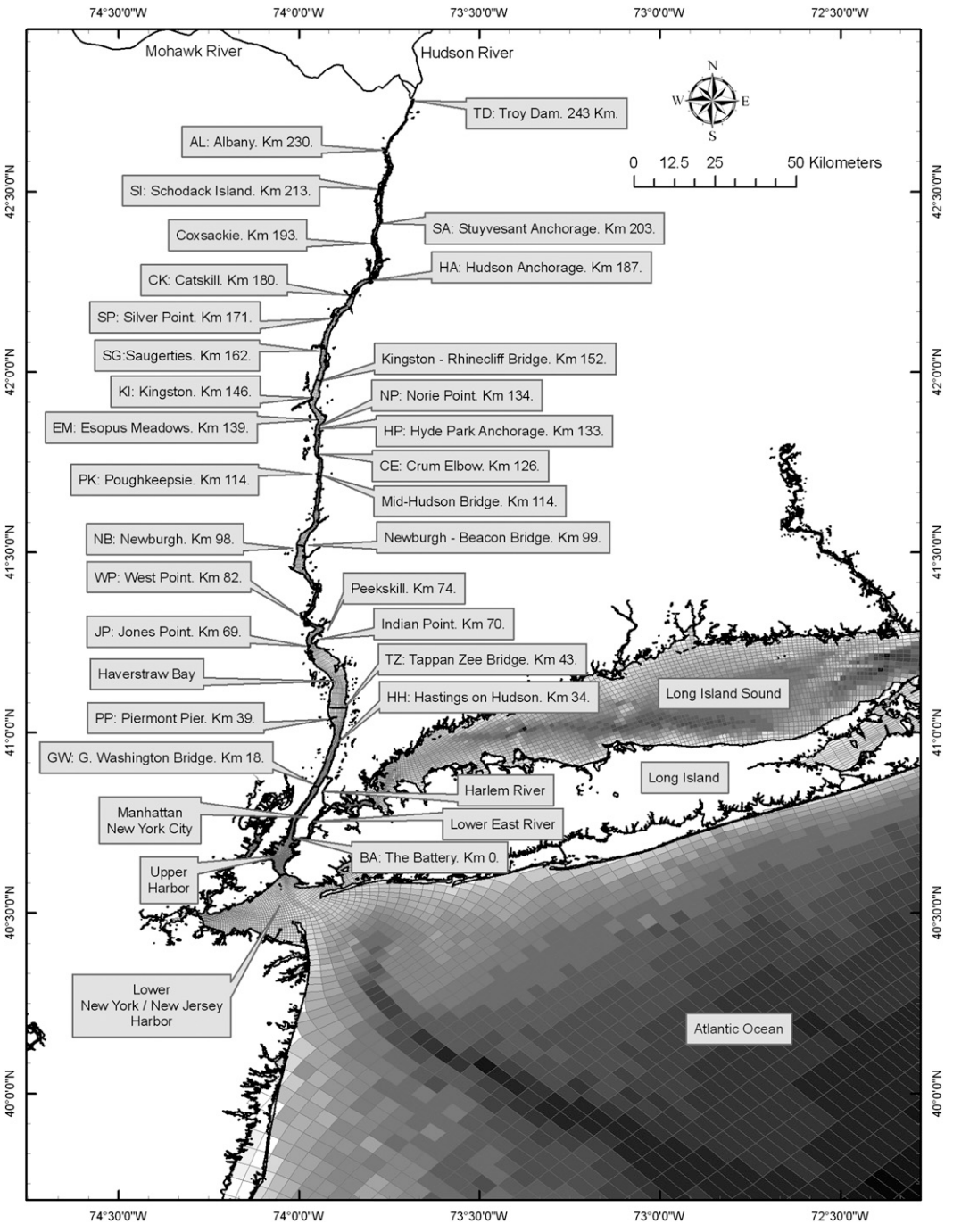

FIG. 1. Map of the HRE. Places and stations referenced in this study are shown with corresponding river kilometers. The NYHOPS model grid resolution is also shown; scales of gray increase per bathymetric depth (note the Hudson River canyon, outside the New York/New Jersey Harbor).

K1 = 12.8 cm, O1 = 7.6 cm, Q1 = 1.5 cm, M4 = 10.6 cm, and M6 = 4.4 cm. Tidal asymmetry also increases toward the head of the tidal Hudson River (M4/M2 = 14.8% at Albany, with a relative phase 2M2 − M4 = 92.1°), indicating a very short and strong flood there created by the longer falling than rising tide (Georgas 2010). In terms of currents, in the estuarine part of the river, the depth-averaged M2 tidal current amplitude increases from about 50 cm s^{-1} in the upper New York Harbor to over 80 cm s^{-1} and is approximately 1 m s^{-1} at the surface waters west of Manhattan and then drops again to about 50 cm s^{-1} near Poughkeepsie (Georgas 2010).

b. USCG ice-breaking operations in the Hudson

U.S. Coast Guard (USCG) sector NY is responsible for keeping the Hudson River navigational channels open to commercial traffic during the official ice-breaking season between 15 December and 31 March each year. During this period and for at least the past 10 yr (E. Munoz 2011, personal communication), daily ice reports are generated by officers onboard the ''140 ft'' ice breakers and ice-breaking tugs that service the Hudson. The reports include the general types of ice, visually observed ice thickness, and approximate percent ice cover of the navigational channel at the end of each service day, within given regions of the river, and at known choke points (CPs; potential ice jam sites).

c. The New York Harbor Observing and Prediction System

The New York Harbor Observing and Prediction System (NYHOPS; Bruno et al. 2006) utilizes observations from sensors as well as federal agency forecasts, to create input forcing to a three-dimensional (3D) hydrodynamic operational forecast system (OFS). The model code, Stevens Estuarine and Coastal Ocean Model (sECOM), is a descendant of the Princeton Ocean Model (Blumberg and Mellor 1987) and the Estuarine and Coastal Ocean Model with Sediment Transport (ECOMSED; Blumberg et al. 1999; Georgas et al. 2007; Bhushan et al. 2010; Georgas 2010). The NYHOPS model grid includes the HRE (Fig. 1). The model has been extensively validated against observations of all its predictive fields during a 2-yr period (Georgas and Blumberg 2010).

The NYHOPS model is forced in the offshore by tidal and tidal residual water level and long-term thermohaline conditions; at the surface with a meteorological wind stress and heat flux submodel; at the bottom with quadratic friction; and internally with thermodynamic inputs from river, stream, and water pollution control plant discharges and thermal power plant recirculation cells (Georgas 2010). With regard to the bottom shear stress boundary condition in particular, the quadratic formulation is used,

$$\boldsymbol{\tau}_b = \rho_0 |\mathbf{v}_*| \mathbf{v}_*. \tag{1}$$

In the absence of waves, the bottom shear velocity $\mathbf{v}_*$ is approximated as

$$|\mathbf{v}_*| \mathbf{v}_* = C_D |\mathbf{v}_b| \mathbf{v}_b, \tag{2}$$

with the logarithmic law of the wall used to define the bottom drag coefficient C_D for flow assumed fully turbulent,

$$C_D = \max\left\{ C_{D,\min}, \left[\frac{1}{\kappa} \ln\left(\frac{D + z_b}{z_0} \right) \right]^{-2} \right\}, \tag{3}$$

where κ is the Von Kármán constant (0.41), z_b and $\mathbf{v}_b$ are the bottommost grid level and corresponding velocity, and D is the instantaneous total water column depth. In NYHOPS, the hydrodynamic bottom roughness z_0 is set to 1 mm throughout the model domain (as in Blumberg et al. 1999) and the minimum drag coefficient $C_{D,\min}$ is also kept spatially constant and set to 3×10^{-3} throughout, similar to Blumberg and Pritchard (1997). In deep water, outside the fetch-limited HRE, the bottom drag from (3) is adjusted for the influence of the wave bottom boundary layer through the theory of Grant and Madsen (Grant and Madsen 1979; Georgas et al. 2007; Georgas 2010).

3. Methods

a. Semiquantitative analysis of USCG daily ice reports

Daily ice reports for the last four winters were provided by the USCG. Although ice reports are filed daily, the values in them are updated less frequently, as ice breakers move to service different river stretches on different days, and even then some values may be reported as unknown. The reports were transcribed into a database of ice type, percent navigational channel area covered, and mean ice thickness (mean of the noted thickness range) for each day with USCG observations and each river segment. Time series of daily mean statistics were summarized as an area-weighted average for the regions of the river north of West Point. These statistics provide semiquantitative insight on winter ice cover conditions in the Hudson.

b. Analysis of observations of water levels

The NYHOPS-supporting observational database includes datasets from the National Ocean Service (NOS), the U.S. Geological Survey (USGS), and the Hudson River Environmental Conditions Observing System (HRECOS) from sensors sufficiently protected and placed to measure water levels and currents during icy periods. Available records were retrieved for the NOS station at BA, five USGS stations (water level HH, WP, PK, and AL and vertical current profiles PK), and four HRECOS stations (water level GW, PP, NP, and SI) in the HRE between April 2007 and March 2011 (locations in Fig. 1). The observations at AL are shown in Fig. 2.

With the exception of the NOS gauge at BA for which tidal epoch harmonic constituents have been published,

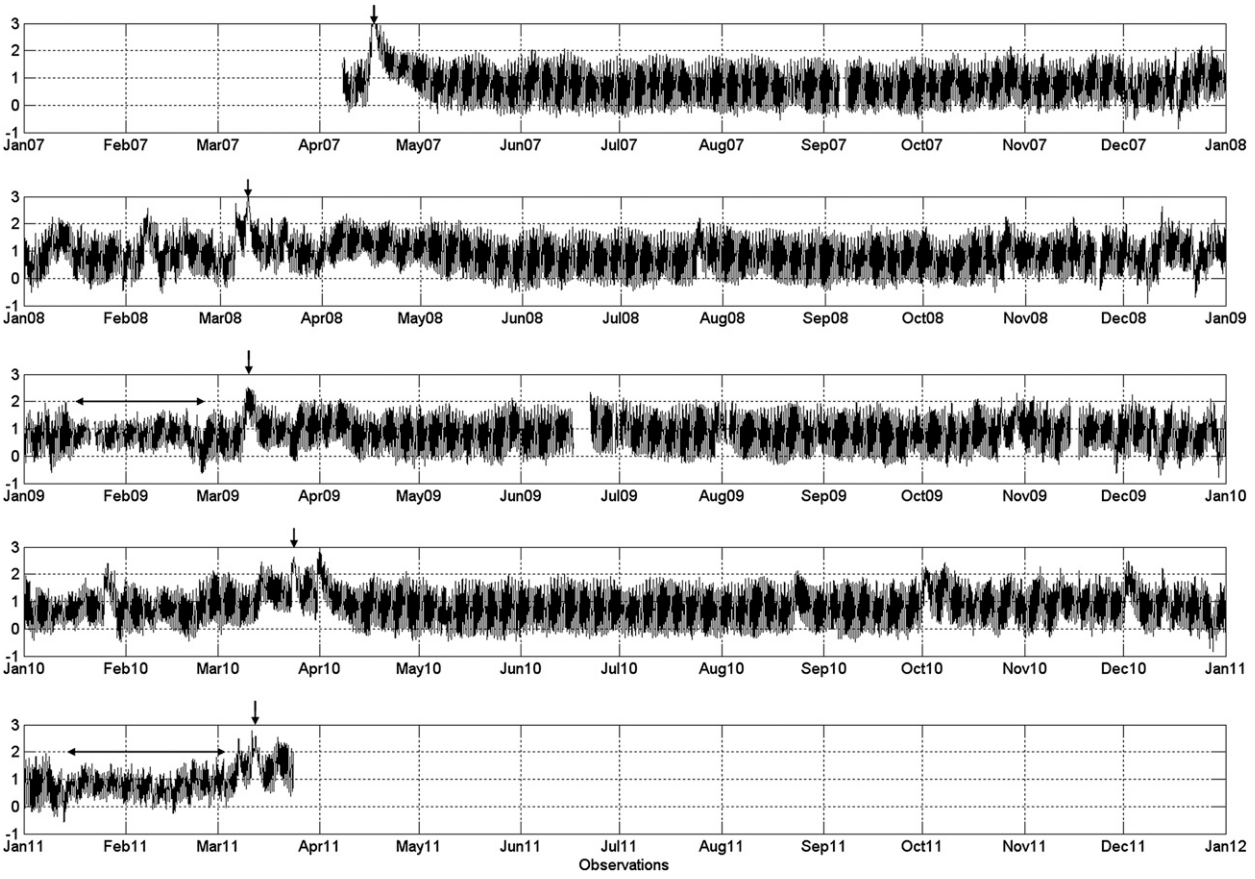

FIG. 2. Observed water level (meters) at Albany, showing significantly smaller tidal ranges in some winters (horizontal arrows), especially around J–F for 2009 and 2011. A number of spring freshets (vertical arrows) are shown (e.g., 17 Apr 2007 and in MAR for 2008–11).

standard NOS tidal harmonic analysis (Foreman 2004) was performed for water level records at these stations, serendipitously, for a period that included a mild winter when a significantly smaller amount of ice formed in the HRE (7 September 2007–22 November 2008). Based on the extracted harmonic constituents, tidal prediction was then carried out into the future. Upon calculation of the residual (observed water level minus the astronomical tide prediction), tidal modulations were found in that residual. These were especially pronounced at AL not only during the freshet months (well-known tide–river flow interaction) but mostly during winters with ice cover in the HRE (Fig. 3).

Shorter-term tidal harmonic analysis, including 95% confidence intervals based on the tidal residual spectrum, was performed using T_TIDE (Pawlowicz et al. 2002) for the 31-day periods of 1–31 December (DEC), 15 January–15 February (J–F), and 1–31 March (MAR) at all stations for the past 4 yr. In addition, because the tide at AL was found to be highly nonstationary, continuous wavelet transform (CWT) analysis (Jay and Flinchem 1997; Flinchem and Jay 2000; Jay and Kukulka 2003; Kukulka and Jay 2003) was also performed there, using a MATLAB function originally written by T. Kukulka to examine the modulation of diurnal D1, semidiurnal D2, and quarter-diurnal D4 tidal species and whether it coincided with ice cover events identified from the ice reports.

c. *Barotropic model runs with simulated ice effects*

A deprecated 2D version of the NYHOPS model, solving the depth-averaged external (barotropic) mode of the equations of motion over the HRE portion of the finite-difference NYHOPS grid shown in Fig. 1, was used to independently examine which of three possible ice effects may be the primary cause of the seasonal tidal modulations in the Hudson (as in Morse et al. 2006a): 1) friction under fast ice cover; 2) the possibility of loss of storage by shore-fast, anchored ice along shallow banks and flats, or 3) reduction in the effective depth of the river due to the ice cover volume. The four barotropic simulations are summarized below:

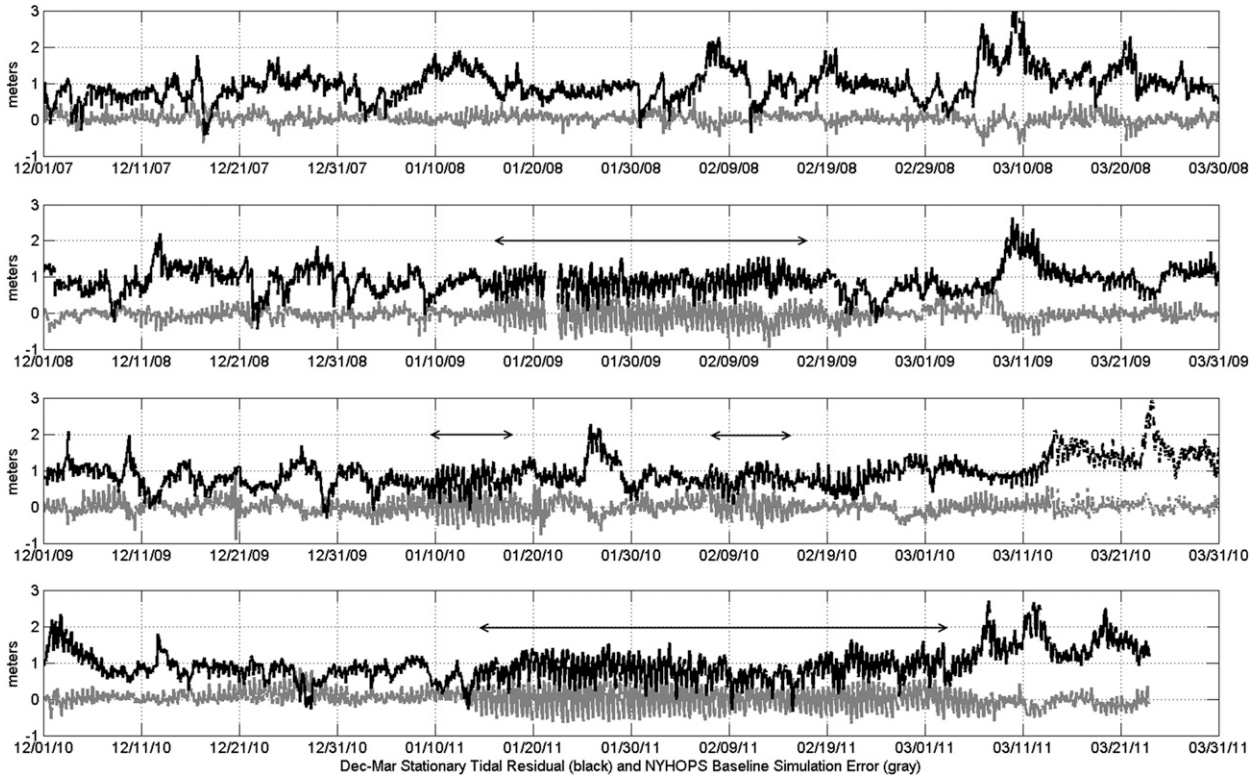

FIG. 3. Observed tidal residual water level at Albany (black) and difference (error) between standard NYHOPS OFS water level prediction and observed water level (gray) for four consecutive winter periods. Note the periods of persistent tidal modulations evident in the water level among extraction of the stationary astronomical tide, coincident with periods of high error in the standard model.

Case I: A baseline run was set up with astronomical tidal forcing (observed S2, M2, N2, K1, P1, and O1) applied at the open boundary at the Battery and a 240 $m^3 s^{-1}$ Hudson inflow at the Troy dam, representative of estimated J–F 2011 streamflow conditions (~260 $m^3 s^{-1}$). The quadratic drag coefficient C_D was set equal to 2.5×10^{-3}. Note that, for a barotropic run, $\mathbf{v}_b$ in Eq. (2) is replaced by the depth-averaged velocity rather than bottom velocity and that $C_D = C_{D,\min}$ in (3).

Case II: Here, C_D was raised from the baseline 2.5×10^{-3} (bottom only) to $C_{D,\text{total}} = 10 \times 10^{-3}$, at the area identified from the USCG ice reports as prone to ice cover in the winter, north of Peekskill all the way to Troy (Fig. 1). In a 2D barotropic run, this is equivalent to using an additional ice–water drag coefficient $C_{D,\text{ice}}$ of 7.5×10^{-3} acting on the depth-averaged flow, a value on the average side of literature values (St. Laurent et al. 2008; Langleben 1982; Pease et al. 1983; Madsen and Bruno 1986; Parthasarathy and Muste 1994; Savant et al. 2009, among others).

Case III: Loss of storage by shore-fast top-to-bottom frozen ice in the areas of the Hudson River shallower than a nominal 3.5 m at mean water level.

Case IV: An effective shallowing of the whole river north of Peekskill by a nominal 1 m due to ice cover volume.

The high values used in cases III and IV were chosen for illustration. Each simulation lasted 10 days; all 2D runs reached stationary state.

d. 3D baroclinic NYHOPS runs with ice cover friction

For the 4-yr period that in situ observations were available, standard NYHOPS version 3 (v3) OFS model predictions were retrieved at the abovementioned observation locations along the HRE. The simulated 10-min-averaged records were compared to the observations. The standard OFS model did not perform well in the Hudson during the last three winters (Fig. 3 shows elevation error at Albany). The author hypothesized that model predictions suffered because of the same reason as the astronomical tide predictions, seasonal ice cover, which is neglected in the operational model.

To test this, a simple surface ice drag quadratic law was added to the sECOM model code to approximate surface stress $\boldsymbol{\tau}_{s,\mathrm{ice}}$ from the presence of a stalled ice cover,

$$\boldsymbol{\tau}_{s,\mathrm{ice}} = \rho_0 C_{D,\mathrm{ice}} |\mathbf{v}_s| \mathbf{v}_s, \tag{4}$$

where the ice–water drag coefficient $C_{D,\mathrm{ice}}$ was set to a constant 7.5×10^{-3} through calibration in the midwinter 2011 period (within a tested range from 5.0×10^{-3} to 10.0×10^{-3}) for the complete river run north of Peekskill, New York, to the federal dam at Troy, New York. Also, $\mathbf{v}_s$ in (4) is the horizontal water velocity at the surface-most grid level. Note that, by adopting the use of (4) and not a more complete formulation that substitutes $\mathbf{v}_s$ with a relative water to flowing ice velocity, the simulated ice cover is assumed to be horizontally fast, irrespective of ice type, thickness, wind stress, etc. This is consistent with observations made by the author on 17 February 2011 onboard the USCG icebreaker *Sturgeon Bay* between Kingston, New York, and Crum Elbow (Fig. 1). Though this is undoubtedly a simplification, it is quite instructive as will be seen in the model results for periods of concentrated ice formation on the HRE. The NYHOPS model with surface stress based on (4) in the specified area was run for two recent midwinter periods with pronounced ice effects: J–F of 2009 and 2011. Results were then compared to in situ observations and the NYHOPS OFS baseline run.

4. Results

a. *Ice cover distribution in the Hudson River during the last four winter seasons*

Average statistics over the last four ice seasons (Table 1; ice season defined here from the time ice shows up in the river, until it is last mentioned in a USCG report) show that the percent of area covered with ice increases significantly as the river narrows at Peekskill, south of West Point, and all the way north to the port of Albany; the stretch between Albany and Troy was relatively undersampled (Table 1). For the length of the river north of WP to TD, the area-weighted grand mean percent of river channel area covered with ice I_A was 55%. The area-weighted grand mean ice thickness I_t was 10.6 cm. Comparison of time averages and medians (Table 1) shows skewed distributions almost everywhere: north of WP, usually a larger amount of area is covered than the mean would imply, whereas south of WP the reverse holds true. The maximum reported local thickness of the ice field during the four years was 45.7 cm (mean of 30.5–61.0 cm reported local range) recorded on 24 January 2011 between Kingston and Catskill, after a 4-yr minimum overnight low air temperature of −25°C was recorded at Albany. The 66-km-long river run between Poughkeepsie and Catskill appears to be the most ice covered, with four known choke points situated there (CE, HP, EM, and SP). The area-weighted average thickness of the 161-km-long stretch of tidal river navigational channels north of WP exceeded 25 cm five times. Based on these findings, ice drag was included in the numerical experiments for the whole length of the river north of Peekskill to Troy.

TABLE 1. Overall ice cover distribution statistics in various reaches of the navigational channels and known CPs (acronyms as in Fig. 1) of the tidal Hudson River, calculated based on the USCG ice reports, where and when available (see sample days count for thickness n_t and percent area covered n_A), for four consecutive ice seasons, beginning with 2007/08 and ending with 2010/11. Here, an ice season is defined to start the day before ice is first reported on a USCG report and end the day after the last ice is reported on the river. Here, I_t = ice thickness; I_A = ice cover area; overbar denotes four-season-mean values; $\hat{I}_t$ is the median ice thickness among the four seasons; $\hat{I}_A$ is the median ice-covered area among the four seasons; and, $I_{t,\max}$ is the center point of the maximum thickness range reported at a particular day and place. General direction of places is from south (GW) to north (TD).

Reach or CP	$\bar{I}_t$ (cm)	$\bar{I}_A$	$\hat{I}_t$ (cm)	$\hat{I}_A$	n_t	n_A	$I_{t,\max}$ (cm)
Around GW	0.7	4%	0.0	0%	124	130	16.5
TZ–JP	2.6	18%	0.0	0%	128	151	15.2
JP–WP	2.8	19%	0.0	0%	126	147	16.5
CP: WP	8.9	49%	7.6	60%	148	168	30.5
WP–NB	9.0	47%	7.6	50%	158	180	38.1
NB–PK	9.3	52%	10.2	60%	167	186	38.1
CP: CE	10.1	59%	7.6	70%	154	175	38.1
CP: HP (NP)	11.0	58%	10.2	70%	157	174	30.5
CP: EM	13.0	67%	12.7	80%	160	183	38.1
PK–KI	12.3	64%	12.7	70%	173	194	40.6
CP: CP	10.6	59%	11.4	70%	109	131	30.5
KI–CK	11.5	61%	11.4	70%	171	194	45.7
CP: HA	10.5	54%	10.2	60%	116	131	40.6
CP: SA	7.3	46%	5.1	50%	85	104	30.5
CK–AL	10.9	50%	10.2	50%	114	153	33.0
AL–TD	6.3	55%	0.0	70%	57	106	33.0

The winter of 2010/11 was the coldest and iciest of the four, in terms of duration, ice-covered area, and thickness (Fig. 4), ending with two significant rainfall/snowmelt events around 6–7 and 12 March 2011 that melted and flushed out the ice. Over 80% of the navigation channels north of WP were covered with over 15 cm of ice in J–F 2011. The winter of 2008/09 was somewhat similar but with less ice cover in December and February (note the longer periods of above freezing temperatures during these months compared to 2010/11; Fig. 4). On the other hand, January 2009 started as being one of the iciest but ended in a period of significant thaw including a heavy-rain/flooding event on 25 January 2010 that was then followed by a refreezing in February, making for a bimodal distribution that season. The winter of 2007/08 was the mildest.

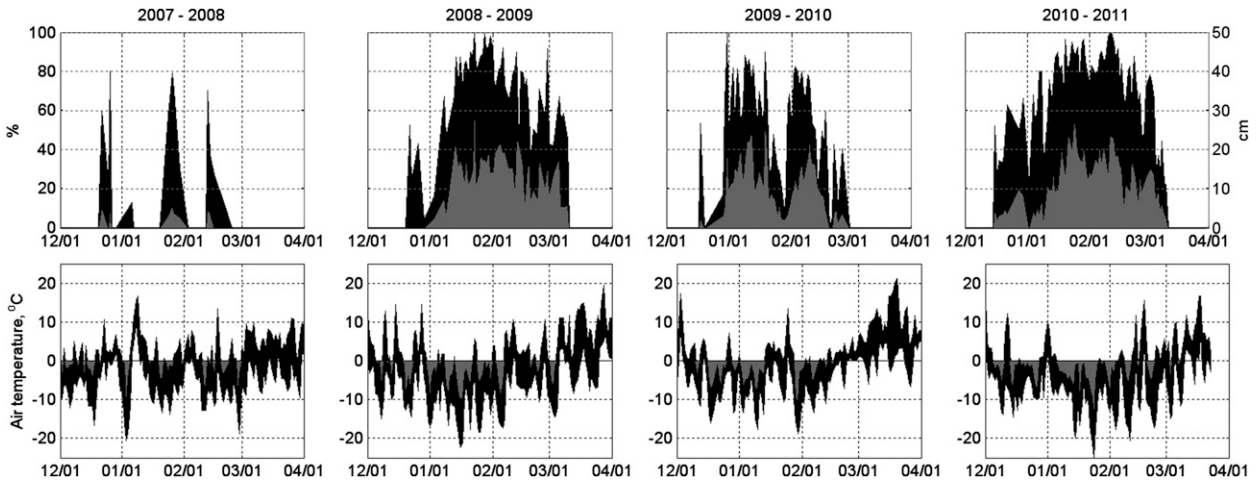

FIG. 4. (top) Area-weighted mean ice field cover (black; 0%–100%) and thickness (gray; 0–50 cm) for the navigational channels of the tidal Hudson north of WP based on the USCG ice reports. (bottom) Daily surface air temperature range recorded at Albany, with subfreezing periods highlighted with gray.

b. Analysis of water level observations

Anomalies for the M2 and M4 are visualized in Fig. 5. The largest changes in tidal amplitudes occur in the J–F periods, especially in the two years with extensive ice cover (winters of 2008/09 and 2010/11, consistent with2 the tidal residual profile in Fig. 3). The amplitudes of all three constituents are significantly different (at the 95% confidence level) in winter months with ice (Fig. 5) at stations WP, NP, SI, and AL. At Albany, the reductions in tidal amplitudes are especially pronounced. Between DEC 2008 and J–F 2009, a 35% reduction in M2, a 44% reduction in K1, and a 42% reduction in the M4 overtide were observed, all statistically significant. The reductions for the icier 2010/11 year were even greater at Albany (42%, 50%, and 55%, respectively). At SI, the amplitude reductions were similar to AL. Further downstream, at NP, the amplitudes were also decreased but less. No statistically significant difference was found at PK. However, at WP, an increase in amplitude was found, significant at the 95% level for the icier 2010/11 winter, not only for the M2 tide (Fig. 5) but also for the N2 and S2 semidiurnal constituents (not shown). It will later be shown that this is due to partial reflection of the incident wave by the ice cover. Phases were also significantly different among consecutive periods, with high and low waters occurring on the average 50 min later during the midwinter periods of 2009 and 2011 than predicted by the stationary long-term tidal analysis.

The results of the CWT analysis for the 4-yr record are shown in Fig. 6. The stationary tidal residual is obviously affected by the Hudson River freshwater input, but with significant variability from day to day in both tidal and subtidal frequencies (Fig. 6a). The D1, D2, and D4 species all resolve these significant modulations throughout the year. These modulations are very pronounced for the D1 diurnal, making the signal hard to decipher based on observations alone (Fig. 6b), as also found in Godin (1999) for the St. Lawrence and Jay and Flinchem (1997) for the Columbia.

Week-to-month-long reductions in the primary D2 semidiurnal species (but also visible in the D4) are correlated to periods of ice field formation in the river (included in Fig. 6c, with arbitrary units). Significant, short-lived decreases in D2 (Fig. 6c) usually coincide with large freshwater events (for example around 10 March 2008 and 24 March 2010). For the record as a whole, D2 is inversely correlated with increased periods of Hudson streamflow, transferring energy to D4, with the $(D4/D2)^2$ tidal asymmetry strength (Fig. 6e) following the seasonal changes in the Hudson freshwater flow, whereas the relative asymmetric phase, $2D2 - D4$ is near constant throughout the record (Fig. 6f).

c. Barotropic model runs with simulated ice effects

Short-term (24.82 h) results of the 2D barotropic HRE simulations, including observations for qualitative comparisons, are shown in Fig. 7. Compared to the baseline case (case I), case II is the only one that reproduces the observed amplitude reduction and phase progression at the northern stations (SI and AL) but also an increase in amplitude at WP. Case III (shallow storage loss) increased the range at AL and retarded the phase, opposite to observations. Case IV (effective shallowing due to ice draft) had similar effects to case II at the northern stations, but not as pronounced, even though the ice volume

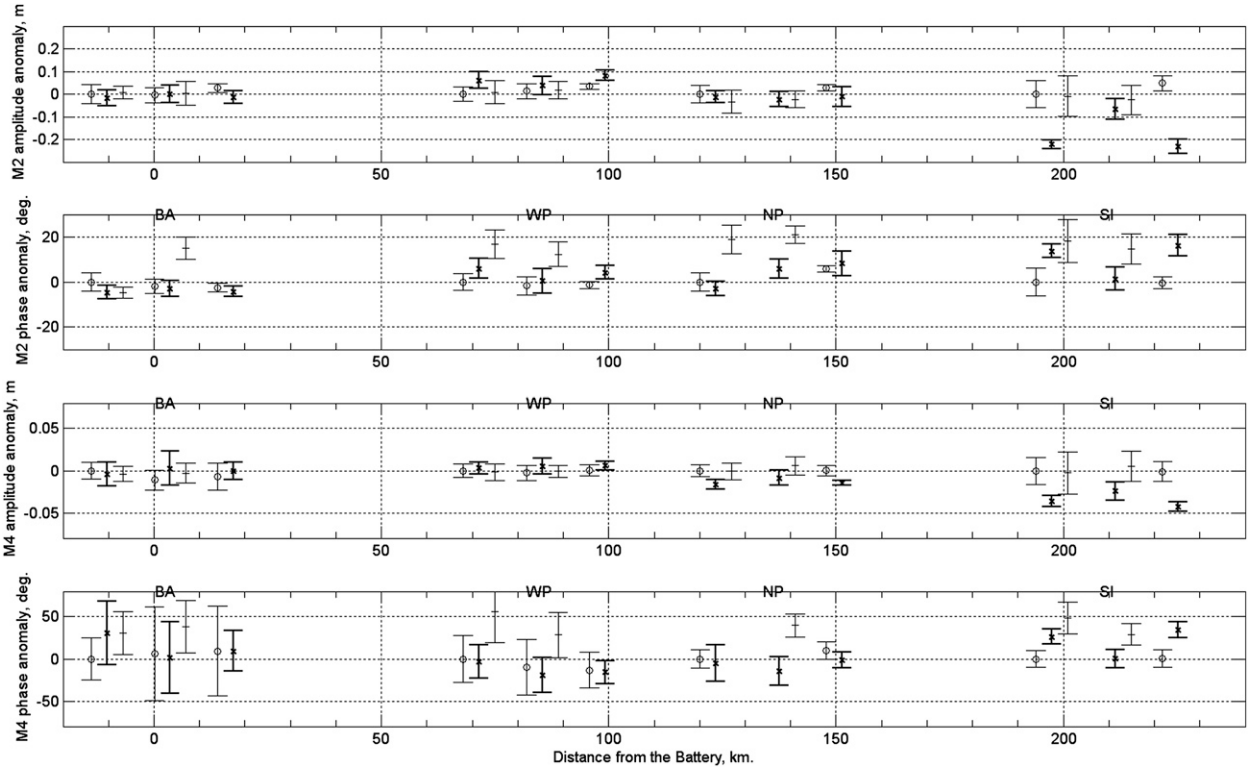

FIG. 5. M2 and M4 constituent anomalies (and 95% confidence intervals) extracted from short-term harmonic analysis of eight (where available) 31-day periods at four Hudson River stations (BA, WP, NP, and SI). From left to right, centered around a station location: DEC 2008, J–F 2009, and MAR 2009; DEC 2009, J–F 2010, and MAR 2010; and DEC 2010, J–F 2011, and MAR 2011. DEC is shown by open circles; J–F is shown by bold Xs; and MAR is shown by plus signs. Note the decrease in M2 tidal amplitude at SI but also the increase in M2 amplitude at WP for the two years with the highest ice field cover (J–F of 2009 and 2011). Significant phase shifts are also visible, as well as the decrease in M4 amplitude at the SI station.

was assumed 2 times larger than the maximum observed. Also, case IV retarded the phase at GW, which is also not seen in the observations.

Comparison of case II to a numerical experiment of an HRE-like tidal embayment without a river inflow revealed that the inflow raises the head elevation at the northern part (not shown); increased ice friction magnifies that upstream pressure gradient slope, by about 20 cm. This effect is also found in ice-infested nontidal rivers.

d. 3D baroclinic NYHOPS runs with ice cover friction

Figure 6 includes CWT analysis of the NYHOPS OFS model results at AL without ice friction. The NYHOPS prediction of the major D2 semidiurnal tidal species during ice-free periods has a 4.3-cm RMSE, whereas for ice-infested periods it reached a 22.1-cm RMSE. This may be compared to a 12.3-cm standard deviation of the observed D2 species at AL for the 4-yr record. Results were similar for D1 and D4 and for the water level signal as a whole, with the NYHOPS OFS model performing poorly in periods with ice. The reader may also note that the NYHOPS model is shown to generally overestimate D4 modulations throughout the 4-yr record at AL, overproducing D4 and overadjusting the relative 2D2 − D4 phase during freshets. Even though individual constituent phases shift and individual constituent amplitudes vary, the relative asymmetric phase remains almost constant throughout (Fig. 6). M4/M2 and 2M2 − M4 were statistically equal for adjacent winter months at all stations.

Model errors for the J–F 2011 NYHOPS simulations with and without ice are shown in Fig. 8. Upon inclusion of surface ice friction, the errors drop significantly, not only at the upstream SI and AL stations but also at the WP and the GW station, with the latter being in an ice-free area 56 km south of Peekskill, the southernmost point where the ice field friction was imposed. The smallest effects are found mid-river (at PK) and at the mouth (BA). Because the ice–water drag coefficient was calibrated for the 2011 model run, the differences (and RMSE) between observations and a NYHOPS

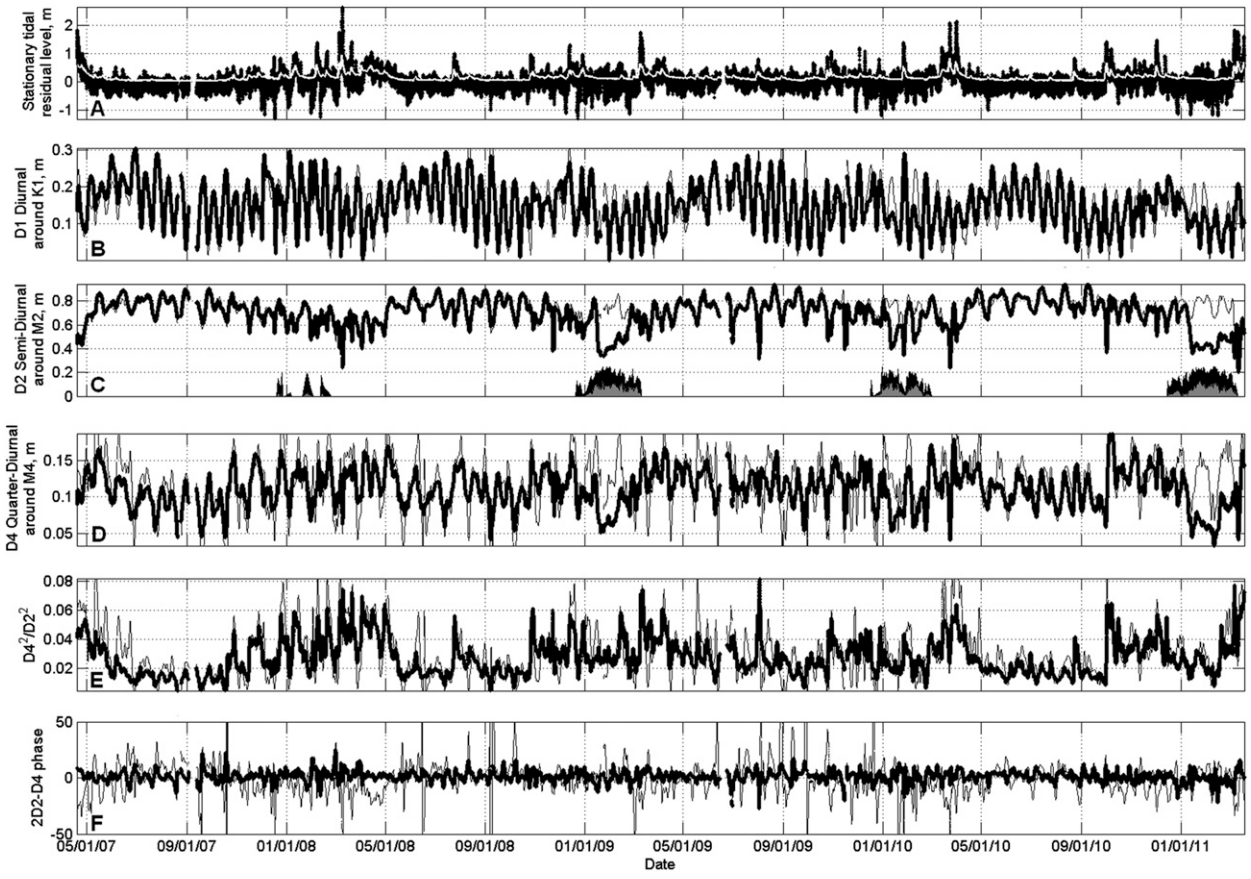

FIG. 6. CWT analysis of nearly four years of water level observations at Albany. (a) Stationary tidal residual water level (black line) and estimated Hudson streamflow over the Troy Dam at Green Island, New York (white line, normalized by the maximum flow in the period, for visual comparison). (b) D1 diurnal species around the K1 astronomical frequency (thick line is from observations and thin line is from NYHOPS standard OFS model without ice). (c) D2 semidiurnal tidal species around the M2 astronomical frequency (thick line is from observations and thin line is from NYHOPS; percent ice cover and thickness as in Fig. 4 also shown, in arbitrary units, for visual comparison) (d) D4 quarter-diurnal species around the M4 overtide frequency (thick line is from observations and thin line is from NYHOPS). (e) Species asymmetry strength $(D4/D2)^2$ from observations (thick line) and NYHOPS model (thin line). (f) Demeaned species asymmetry relative phase 2D2 − D4 from observations (thick line) and NYHOPS model (thin line). Also note the differences in scale of tidal species [y axis of (b)–(d)].

run using the same ice–water friction drag coefficient (7.5×10^{-3}) for the ice-covered period J–F 2009 are presented in Fig. 9. RMSE reductions are strikingly similar, again even at a station (HH; Fig. 1) in the ice-free part of the river. However, unlike in the 2011 run, residual modulations in the NYHOPS error remain after including ice–water friction in the beginning and end of the period (Fig. 9, right).

The resulting significant changes in the tidal ranges and tidal propagation due to ice friction are visualized for the whole HRE from the BA to TD in Fig. 10 (top). In the seasonally ice-covered regions north of Peekskill, depth-averaged tidal currents (Fig. 10, bottom) decrease significantly, from 20% to 50% or more. This reduction of the tidal current relative to the mean river flow leads to unidirectional currents from Troy all the way south to the port of Albany: As the amplitude of the tidal current decreases to approximately 15 cm s^{-1} or less north of Albany because of ice cover friction, the weakened flood current is unable to reverse the midwinter Hudson River inflow speed there of 240 m^3 s^{-1}/(5.7-m mean depth × 270-m mean width) ~ 15 cm s^{-1}. Interestingly, south of river-kilometer (R-km) 60, at the estuarine portion of the river, currents increase by about 10%. If ice cover volume is included as a secondary effect to friction, the decrease of tidal currents should be reduced due to the transect area being smaller by up to 5% (50-cm maximum observed ice thickness for a 10-m spatial average river depth).

Figure 11 shows 3D baroclinic NYHOPS model current results with surface ice friction compared to 72 h of observed ADCP current profiles at PK. The vertical

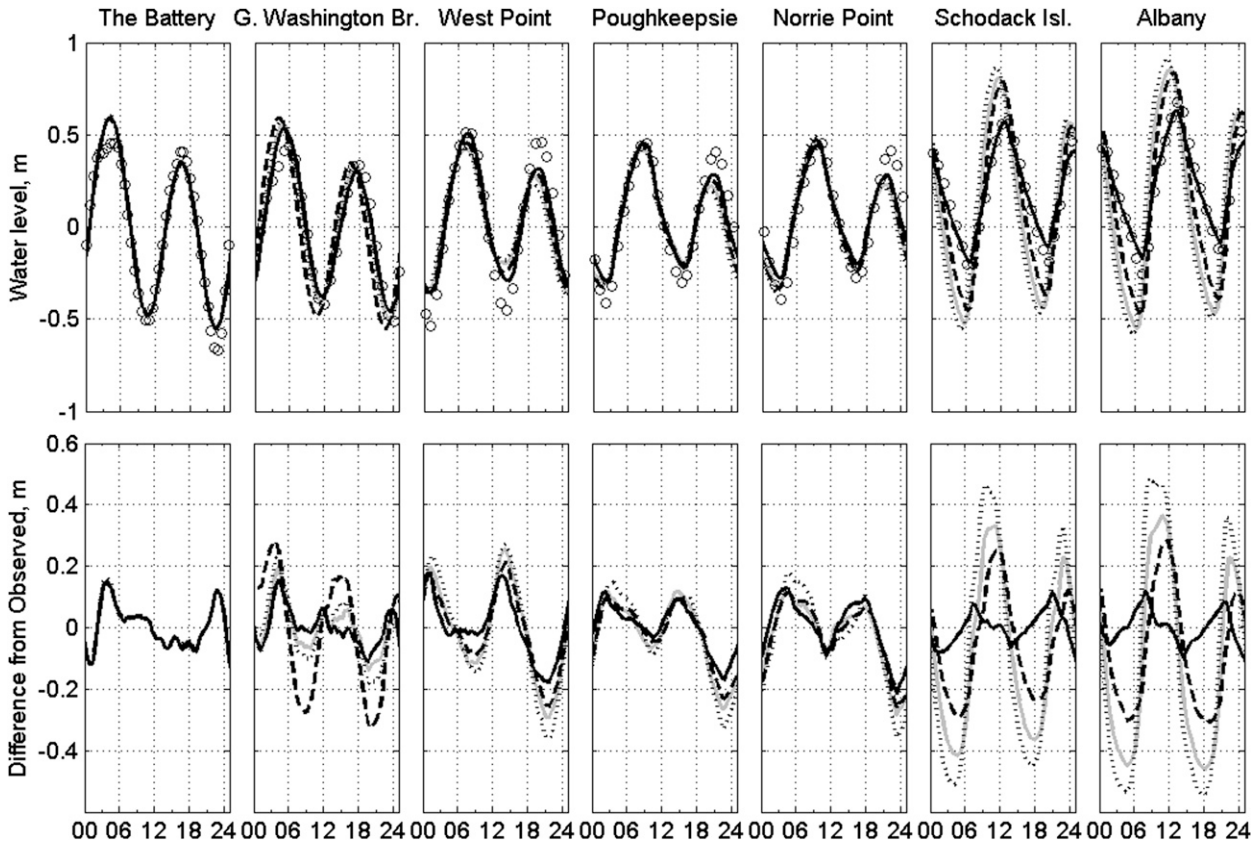

FIG. 7. Predicted water levels at seven HRE locations based on the four barotropic Hudson River model cases described in the methods section: (i) baseline (gray solid line), (ii) increased friction (black solid line), (iii) storage loss (dotted line), and (iv) ice cover volume (dashed line). (bottom) Also shown are the differences of runs I–IV from observations (open circles) made on 15 Jan 2011 (87% ice cover and 9.6-cm average thickness, from WP to TD; USCG reports) after removal of slow meteorological effects (removal of 34-h low-pass-filtered signal).

current profile under the horizontally fast ice field becomes parabolic rather than the typical open channel logarithmic profile. Maximum currents along the principal current direction (PCD) of approximately 50 cm s^{-1} occur just below middepth and decrease toward both the bottom and the surface. RMSE between simulated and observed currents is 6 cm s^{-1}. Without ice–water friction, the operational NYHOPS OFS predicted a logarithmic profile at PK with maximum current at the surface of 80 cm s^{-1} for the same period and an RMSE of 17 cm s^{-1} (not shown). Similar results with regard to currents at PK were found in the 2008/09 simulations: After inclusion of the surface friction, the RMSE dropped from 16 to 7 cm s^{-1} during that midwinter simulation period, and the current profiles (both observed and simulated) were parabolic at times. It should be noted that PK lies in a region of the river (starting from about NB and ending at CE; Fig. 1) that may at times not be covered by ice while the rest of the WP to TD section of the river is. During such times, the current profile at PK was logarithmic, but the currents were found to be significantly attenuated compared to ice-free periods.

5. Discussion

The presented results highlight the difficulty of searching for cause and effect relationships through harmonic analysis of river tides. The observed variability in the tidal constituents from month to month over the winter period is a clear indication of nonstationary river processes. The ''traditional'' river tide nonstationarity caused by quadratic friction and streamflow–tide interaction [in tandem with the interference cycles of M2 and S2 (14.8 days) and of M2 and N2 (27.6 days) and the nonlinear generation of overtides and compound harmonics] contributes greatly to the phase modulations, especially in the March freshet periods. It is out of the scope of this paper to describe all the oscillations of the components within a year (for an in-depth discussion, see, e.g., Godin 1999; Kukulka and Jay 2003). The focus here is on ice–tide interaction.

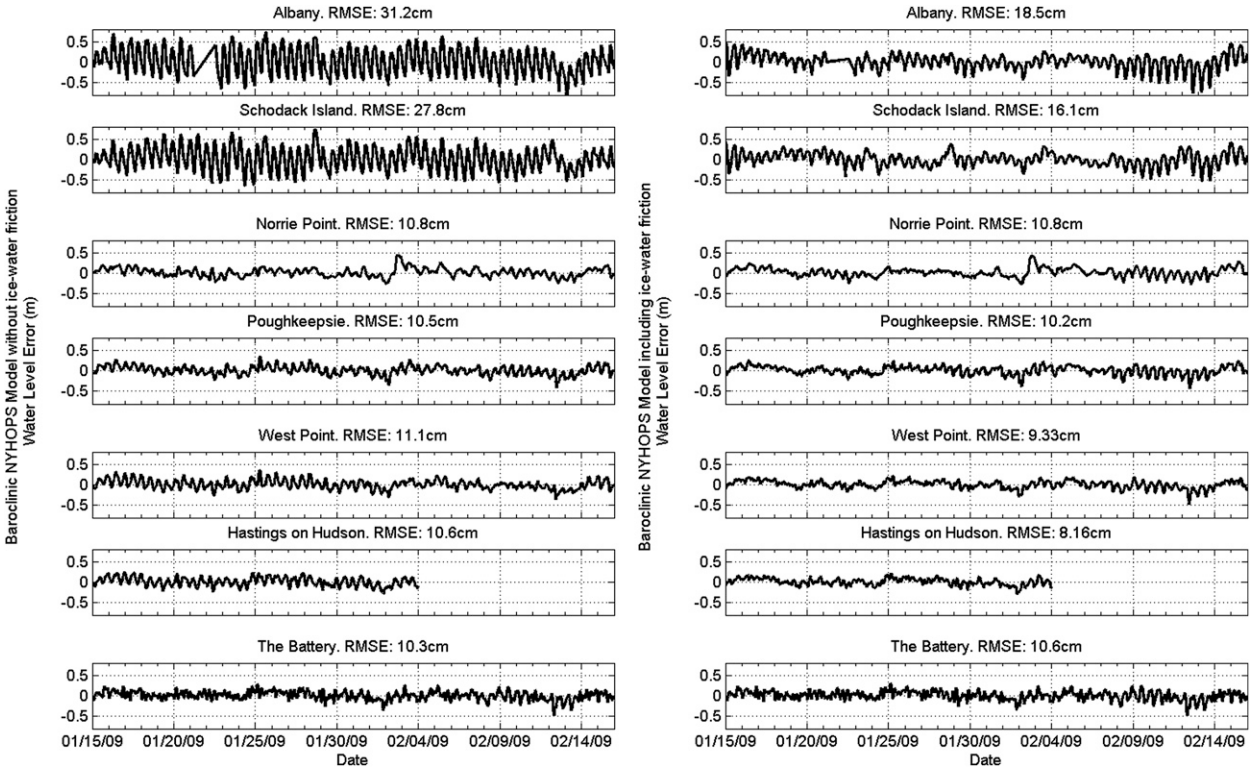

FIG. 8. Differences between observed and simulated water level at seven HRE stations for J–F 2011. (left) Standard NYHOPS OFS model. (right) NYHOPS model with surface ice cover friction. RMS error statistics for the 31-day period in 2011 are also shown.

The nonstationary character of the tide at Albany is better illuminated by the results of the CWT analysis for the entire analyzed record of observations (Fig. 6). Some of the most sudden and durable episodes are the reductions in the primary D2 species (but also visible in the D4 and obscured but present in the D1) coinciding with the ice cover formation on the river. The decreases of D2 and D4 are rapid, comparable in magnitude to decreases from large freshets in the D2 case, but are much more prolonged and on the order of weeks to months, not days. They coincide with times when the areal extent of the ice cover in the navigational channels between WP and TD becomes greater than 60%–80% weighted average based on the USCG ice breaker reports. This is not a phenomenon of the past 3 yr. A CWT scaleogram created for HRE stations for the year 2001 in an unpublished study of sea breeze effects by P. Orton (2011, personal communication) also shows large attenuations of the D2 species in winter at the upper HRE.

The barotropic model with increased friction (case II) reproduced the observed water level signal the best, in terms of both amplitudes and phase (Fig. 7), giving overall the smallest differences compared to observations, at all stations, compared to the runs with the other possible effects of ice cover. Thus, increase in frictional stress by the winter ice field is the explanation for the sudden reductions of tidal ranges and increase in pressure head in the northern HRE, as well as an increase in tidal range around WP, with smaller changes in the middle and outlet of the river (Fig. 10). In summation then, ice friction in the HRE significantly alters both the local tidal ranges and phases, as well as increases the mean water level setup. Figure 6 hints that ice friction may not significantly affect tidal asymmetry (M4/M2 and 2M2 − M4) in the HRE. There was some evidence of third-harmonic M6 growth under ice, possibly a symmetric effect of quadratic friction in generating odd overtides as in Parker (1984) and Godin (1999), but not significant at the 95% level.

The linear damping modulus and partial reflections may explain both the attenuation and augmentation of tide levels and currents due to ice cover friction in the HRE. The incident M2 wave traveling north is damped linearly under the ice cover (log-linear decrease shown in the Stommel/Redfield nomogram in Fig. 12, left). The reflecting wave off the Troy Dam is thus also much weaker than when ice is not present. Both tidal waves also travel slower under the ice: in the Stommel/Redfield nomogram the reference epoch is taken to be the phase of the M2 tide at the Troy Dam to highlight the effect of wave reflection there, but in reality the phase of the M2

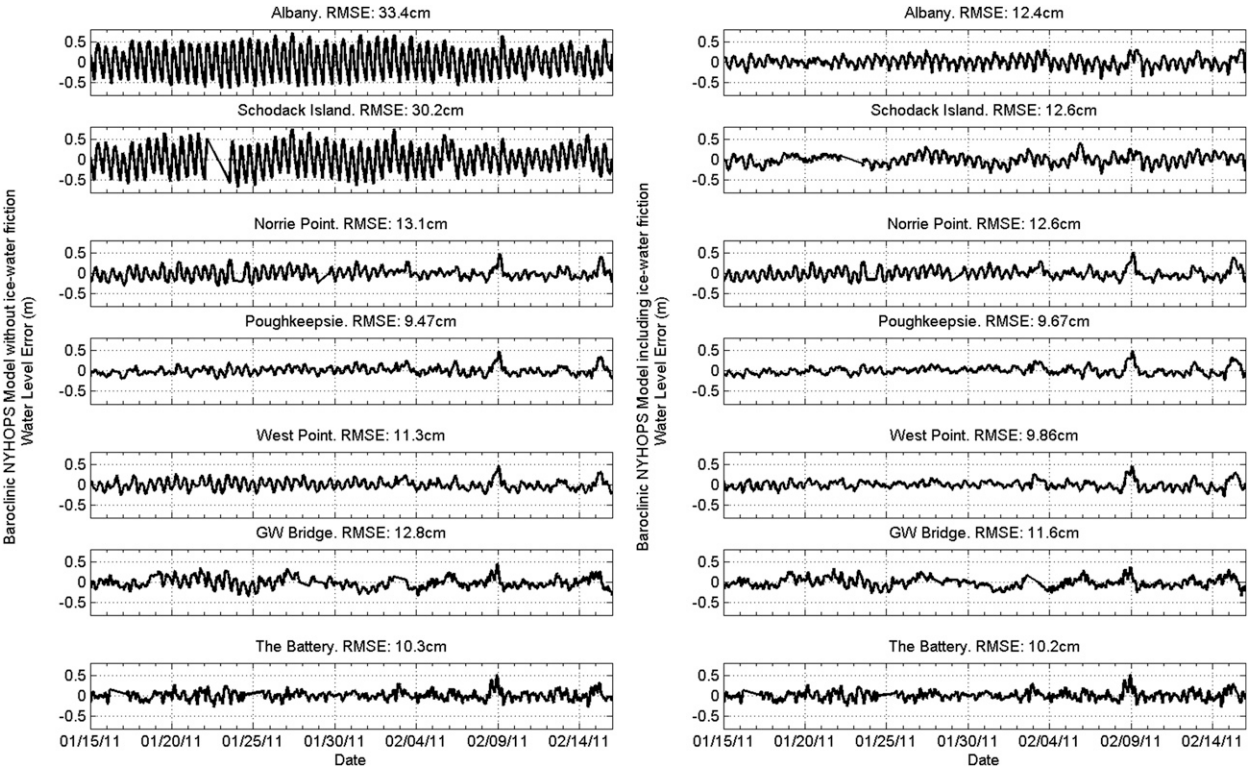

FIG. 9. As in Fig. 8, but for J–F 2009.

wave is approximately equal with and without ice at its point of entry at the Battery; thus, the tidal wave stretches in time because of ice friction toward Troy with a near 20° delay for high waters there compared to the ice-free wave. The ice edge just south of West Point is in the neighborhood of the stretched tidal antinode of the wave, and the local maximum M2 amplitude there may be a combination of these two factors; partial reflection of the tidal wave by the ice cover edge is a probable cause of the local peak.

The Giese/Jay diagram in Fig. 12 (right) further illustrates the effects of local wave reflection. After the tidal wave enters the Hudson at the Battery having attained the form of a progressive wave, the relative phase δ between water level η and transport q increases considerably with a peak near R-km 40 shown in the runs both with and without ice. At the same time, the magnitude of the admittance Y (the response ratio between the transport and water level M2 amplitudes) decreases rapidly. This is most likely due to partial reflection of the incident wave at the entrance to the Tappan Zee around Piermont Pier. A second peak in δ is found at the entrance to Newburgh Bay. Because of the partial reflection of the ice cover at the ice–water edge, the whole δ curve is lifted between the two bay peaks. The significant drop in admittance there shows the conversion of kinetic energy to potential energy as currents are held back and water levels rise (also in Fig. 10). That potential energy is again transferred into kinetic energy as the partially reflected wave moves seaward entering the narrower channels south of Piermont, creating stronger currents and decreased tidal amplitudes all the way south to the Battery, where the wave exits into the upper New York Harbor. At the opposite end of the river, the M2 admittance drops to zero and δ increases to 90°, a standing wave (Fig. 12).

Based on the USCG reports and as expected, a near-linear relationship between mean daily ice thickness and mean daily ice cover area north of WP was found (Fig. 13a). This implies that the ice cover grows and melts both vertically and horizontally in tandem. The operational NYHOPS OFS D2 species overprediction at AL (Fig. 6; but also the underprediction at WP, which is not shown)—found to be primarily due to the neglect of under-ice friction in the model as aforementioned—is correlated to ice thickness (Fig. 13b), with an R^2 value of 0.62. This high R^2 value is remarkable, given the approximate nature of the USCG ice reports upon which the calculation of mean ice field characteristics was based on, and the simplified assumptions in the model. Simple linear R^2 of D2 error to each variable, forced through zero, was 0.57 for thickness and 0.38 for percent area. The best fit

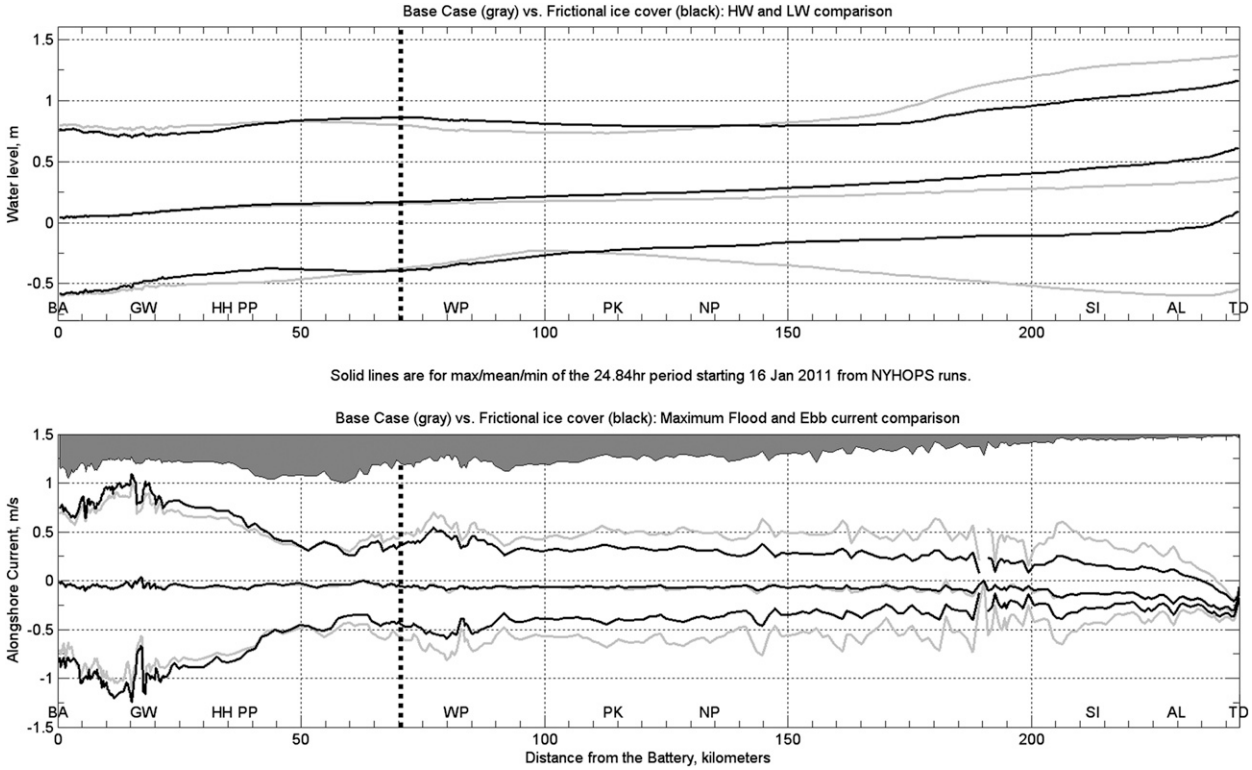

FIG. 10. (top) Along-channel water level and (bottom) depth-averaged current profile comparisons between the standard NYHOPS simulation (gray) and a NYHOPS run with surface ice cover friction (black). Solid lines are for maximum, mean, and minimum water levels (currents) along the transect for the 24.84-h period starting 0000 EST 16 Jan 2011. The vertical thick dotted line marks the southern boundary of the applied surface friction. The shaded gray area in (bottom) represents the area of the HRE.

(out of several attempted) shown in Fig. 13b is a function of ice thickness similar to the one used for air–ice drag coefficients in numerical models. An apparent ceiling for the contribution of ice thickness to the standard NYHOPS D2 error was found, by fitting, at around 17.7-cm thickness. Above that value, the model error tapered off (Fig. 13b).

The remaining modulations seen in Fig. 9 (right) hint to a more gradual buildup and breakdown of ice–water stress around the start and end of the 2009 run period, consistent with the USCG reports for that year (Fig. 4). This implies that a constant water drag coefficient would be a wrong assumption to use in operational forecast models of seasonally ice-infested estuaries. Morphodynamic changes in the value of $C_{D,\mathrm{ice}}$ have been hypothesized by Prinsenberg and Peterson (2002), who also showed an order-of-magnitude variation of the air–ice coefficient, depending on ice roughness. For seasonally ice-covered estuaries and tidal rivers, $C_{D,\mathrm{ice}}$ needs to be defined through a dynamic relationship with ice field distribution and ice field roughness.

In the baroclinic runs, the calibrated value for $C_{D,\mathrm{ice}}$ appears to be close to maximum for the HRE, at least for the period analyzed. The HRE has a mean depth around 10 m. For a 10-sigma-layer model such as NYHOPS, the current $\mathbf{v}_s$ in (4) is evaluated at 50 cm below ice. Thus, a $C_{D,\mathrm{ice}}$ value of 7.5×10^{-3} corresponds to a hydrodynamic ice roughness $z_{0,\mathrm{ice}}$ of 4.4 mm [Eq. (3), but for the ice–water boundary]. For the measured values of ice thickness in the HRE, this value is consistent with Mellor and Kantha's (1989) model, in which they adopted a linear relationship of ice drag to ice cover area and a $z_{0,\mathrm{ice}}$ linearly dependent on I_t between the limits [0, 5 cm] for I_t = [0, 3 m]. Thus, the Mellor and Kantha (1989) drag formulation may work well in the HRE, but with a lower upper bound. Also, the HRE 4.4-mm bound for $z_{0,\mathrm{ice}}$ would translate to a physical Nikuradse-type roughness, $k_s \sim 30 z_{0,\mathrm{ice}}$, of 13.2 cm. This is close to the value found through fitting to be the maximum mean ice thickness to contribute to the NYHOPS D2 error at AL (17.7 cm; Fig. 13b). There may be a physical reason for this correspondence, because the ice in the Hudson may for some natural reason not be rougher (even though at times thicker) than around k_s of 15 cm. Also, the effect of the USCG ice-breaking operations on the physical roughness of the ice field is not known.

The changes on the tidal hydrodynamics of the HRE impacted by the winter ice regime have important

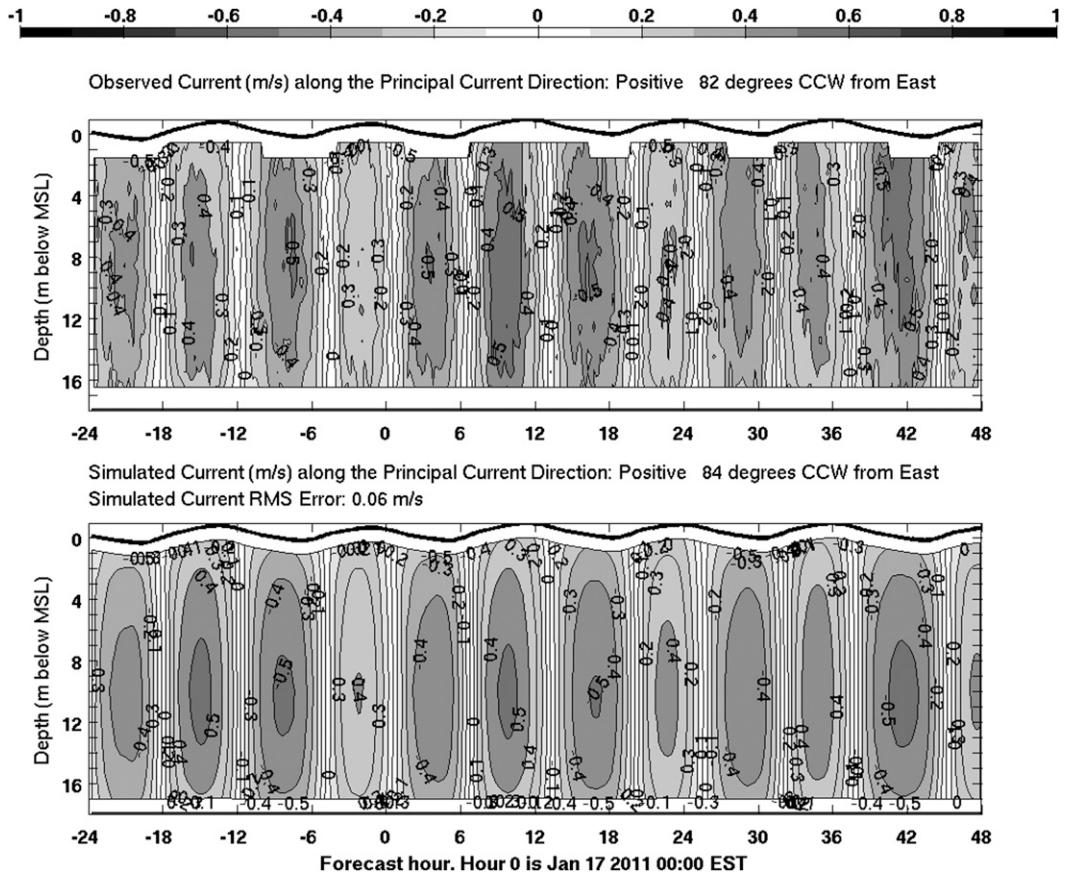

FIG. 11. Comparison between ADCP current profile along PCD observed at Poughkeepsie and NYHOPS model with surface ice cover friction: 16–18 Jan 2011. All current values are in m s^{-1}. Thick black lines denote surface.

implications for environmental engineering studies. For example, increased high water elevations are predicted near and south of WP because of ice cover. During a significant storm event, ocean surge could be superimposed to that higher level and additionally create its own backwater effect at the southern end of the ice field, which has been found to be at the short end of the funnel shaped north Haverstraw Bay. That could increase storm surge elevations coming from the ocean and generate higher potential for flooding there, in addition to the known potential for ice jam flooding coming from upstream choke points. Ice–surge interactions have been studied by only a few investigators and mostly for open coasts (e.g., Murty and Holloway 1985).

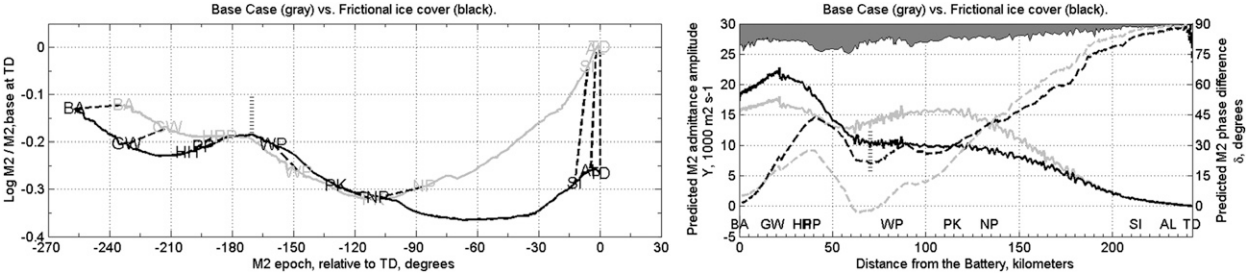

FIG. 12. (left) Stommel/Redfield nomogram (Redfield 1950, 1980) of the M2 tide from the 3D model runs of J–F 2011 with (black) and without (gray) ice cover. (right) Giese/Jay diagram (Giese and Jay 1989) of admittance ($Y = q_{M2}/\eta_{M2}$; solid lines) and relative phase ($\delta = \eta^{\circ}_{M2} - q^{\circ}_{M2}$; dashed lines) from the 3D model runs of J–F 2011 with (black) and without (gray) ice cover. The vertical dotted lines in both diagrams show the seaward extent of the ice cover in the runs with ice. The shaded gray area in the right panel represents the area of the HRE as in Fig. 10.

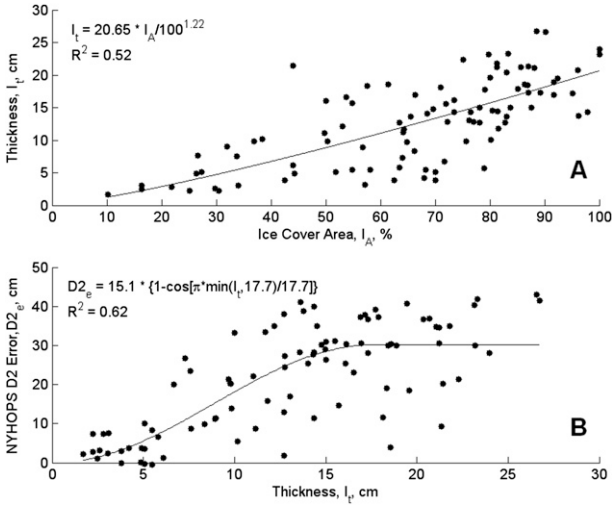

FIG. 13. (a) Regression between mean ice thickness and mean ice cover area based on USCG reports. (b) Least squares fit of standard NYHOPS model D2 error (without ice friction) to the mean daily thickness based on ice reports of the ice field north of WP.

Importantly, the results show that ice field friction has a remarkable impact on the tidal currents throughout the HRE, decreasing them by up to 50%, changing the current profile to parabolic below the ice field, increasing the currents by 10% south of Peekskill, and shifting the current phases and significantly reducing or eliminating the flood current at the upstream section from AL to TD. The latter has also been observed in situ by S. Ireland (Hudson River Pilots Association, 2011, personal communication). It should also be noted that ADCP current observations made by the Beacon Institute for Rivers and Estuaries at AL (pictures were available online, but the data were not available to the author) over the winter of 2010/11 also showed parabolic profiles, decreased currents, and increased current unidirectionality there.

The significant and prolonged decrease of currents under the ice cover and their amplification downstream, with time scales of weeks or months in duration, affect salt intrusion and estuarine dynamics due to changes in vertical shear dispersion and tidal mixing. Amplification of currents in the downstream estuarine section of the river due to partial reflection from the ice cover (Figs. 10, 12) make for neap tides that look almost like ice-free-season spring tides there, and the resulting mixing is similarly more vigorous, affecting stratification and salt transport (as in Geyer et al. 2000). Comparisons of simulated along-estuary tidally averaged salinity (S) profiles from the J–F 2011 runs of the 3D NYHOPS model with and without surface ice cover friction show that, within a few days of surface ice cover having formed between WP and TD, (i) the location of the Hudson River salt front moved downstream by 10–20 km; (ii) the lower estuary downstream of the ice cover edge became less stratified by as much as 20% within 30 km from the Battery, measured as a relative change in dS/dz; and (iii) the estuary became overall fresher, except at its mouth, where its surface waters became saltier. These differences from an ice-free run remained for the rest of the 30 days.

6. Conclusions

It has been shown in this paper that winter-ice-induced tidal modulation episodes (WII-TIMES) occur seasonally because of surface frictional dissipation by ice cover in the Hudson River estuary, altering tidal ranges and tidal currents significantly (both by as much as 50%) for periods of weeks to months at a time. In the tidal Hudson River upstream of the ice field that stops near West Point, tidal currents are greatly reduced under the ice cover and current profiles under the ice become parabolic. Near the edge of the ice field, both tidal ranges and tidal currents increase because of tidal wave reflection. Model simulations showed that tidal flows become smaller relative to the river streamflow near the port of Albany leading to increased ebb dominance there, whereas vertical mixing increased downstream of the ice edge, leading to less stratified conditions in the estuary and limiting salt front intrusion.

Astronomical tidal predictions, tidal river datums on National Oceanic and Atmospheric Administration (NOAA) charts, and operational forecast models such as NYHOPS that do not presently include ice dynamics are compromised. In hindsight, neglect of ice friction explains a major part of the poor NYHOPS RMSE results at the upper HRE stations published in prior studies (Georgas 2010; Georgas and Blumberg 2010; 21.2–22.5 cm at SI and AL), based on a record that included the icy 2008/09 winter period. Instead of day-to-day frictional recalibration, ice thermodynamics (e.g., Mellor and Kantha 1989; though with perhaps a lower upper bound as found herein), an external prediction of ice thickness and concentration (e.g., Morse et al. 2006b), or a drag coefficient data assimilation scheme (e.g., Heemink et al. 2002) would need to be included in a hydrodynamic OFS model such as NYHOPS in order for the model to be able to provide its otherwise highly accurate water level predictions throughout the year, increasing computational demands.

Acknowledgments. Two anonymous reviewers and Drs. A. Blumberg, R. Hires, J. Miller, and P. Orton provided valuable insight and helped improve this paper. The author is very grateful to LCDR E. Munoz,

BM1 M. Lehansky, and CWO K. Moss from USCG sector NY for providing the daily ice reports; LT Dan Everette, the officers, and crew of the USCG cutter *Sturgeon Bay* for their hospitality; D. D'Agostino for help with the transcription of the reports; and Dr. Gary Wall from USGS and Ms. Alene Onion from HRECOS for sharing their data with the NYHOPS system. This work was funded under a subcontract from NYSDEC/NERRS Science Collaborative.

REFERENCES

Abood, K. A., 1974: Circulation in the Hudson estuary. *Hudson River Colloquium,* O. A. Roels, Ed., Annals of the New York Academy of Sciences, Vol. 250, New York Academy of Sciences, 38–111.

——, T. L. Englert, S. G. Metzger, C. V. Beckers Jr., T. J. Groninger, and S. Mallavaram, 2006: Current and evolving physical and chemical conditions in the Hudson River estuary. *Amer. Fish. Soc. Symp.,* **51,** 39–62.

Bengtsson, L., 1996: Mixing in ice-covered lakes. *Hydrobiologia,* **322,** 91–97.

Bhushan, S., A. F. Blumberg, and N. Georgas, 2010: Comparison of NYHOPS hydrodynamic model SST predictions with satellite observations in the Hudson River tidal, estuarine, and coastal plume region. *Proc. 11th Int. Conf. in Estuarine and Coastal Modeling,* Seattle, WA, American Society of Civil Engineers, 11–26.

Blumberg, A. F., and G. L. Mellor, 1987: A description of a three-dimensional coastal ocean circulation model. *Three Dimensional Coastal Models,* N. S. Heaps, Ed., Coastal and Estuarine Sciences, Vol. 4, Amer. Geophys. Union, 1–16.

——, and D. W. Pritchard, 1997: Estimates of the transport through the East River, New York. *J. Geophys. Res.,* **102** (C3), 5685–5703.

——, and F. Hellweger, 2006: Hydrodynamics of the Hudson River estuary. *Amer. Fish. Soc. Symp.,* **51,** 9–28.

——, L. A. Khan, and J. P. St. John, 1999: Three-dimensional hydrodynamic model of New York harbor region. *J. Hydraul. Eng.,* **125,** 799–816.

Bruno, M. S., A. F. Blumberg, and T. O. Herrington, 2006: The urban ocean observatory—Coastal ocean observations and forecasting in the New York Bight. *J. Marine Sci. Environ.,* **C4,** 1–9.

Desplanque, C., and D. I. Bray, 1986: Winter ice regime in tidal estuaries of the northeastern portion of the Bay of Fundy, New Brunswick. *Can. J. Civ. Eng.,* **13,** 130–139.

——, and D. J. Mossman, 1998: A review of ice and tide observations in the Bay of Fundy. *Atl. Geol.,* **34,** 195–209.

Flinchem, E. P., and D. A. Jay, 2000: An introduction to wavelet transform tidal analysis methods. *Estuarine Coastal Shelf Sci.,* **51,** 177–200.

Foreman, M. G. G., 2004: Manual for tidal heights analysis and prediction. Institute of Ocean Sciences, Patricia Bay Pacific Marine Science Rep. 77-10, 58 pp.

Georgas, N., 2010: Establishing confidence in marine forecast systems: The design of a high fidelity marine forecast model for the NY NJ harbor estuary and its adjoining waters. Ph.D. dissertation, Stevens Institute of Technology, 295 pp.

——, and A. F. Blumberg, 2010: Establishing confidence in marine forecast systems: The design and skill assessment of the New York Harbor Observation and Prediction System, version 3 (NYHOPS v3). *Proc. 11th Int. Conf. in Estuarine and Coastal Modeling,* Seattle, WA, American Society of Civil Engineers, 660–685.

——, ——, and T. O. Herrington, 2007: An operational coastal wave model for New Jersey and Long Island waters. *Shore Beach,* **75,** 30–35.

Geyer, W. R., J. H. Trowbridge, and M. M. Bowen, 2000: The dynamics of a partially mixed estuary. *J. Phys. Oceanogr.,* **30,** 2035–2048.

Giese, B. S., and D. A. Jay, 1989: Modelling tidal energetics of the Columbia River estuary. *Estuarine Coastal Shelf Sci.,* **29,** 549–571.

Godin, G., 1986: Modification by an ice cover of the tide in James Bay and Hudson Bay. *Arctic,* **39,** 65–67.

——, 1999: The propagation of tides up rivers, with special considerations on the upper Saint Lawrence River. *Estuarine Coastal Shelf Sci.,* **48,** 307–324.

——, and F. G. Barber, 1980: Variability of the tide at some sites in the Canadian Arctic. *Arctic,* **33,** 30–37.

Grant, W. D., and O. S. Madsen, 1979: Combined wave and current interactions with a rough bottom. *J. Geophys. Res.,* **84,** 1797–1808.

Haidvogel, D. B., and Coauthors, 2008: Ocean forecasting in terrain-following coordinates: Formulation and skill assessment of the Regional Ocean Modeling System. *J. Comput. Phys.,* **227,** 3595–3624.

Heemink, A. W., E. E. Mouthaan, M. R. Roest, E. A. Vollebregt, K. B. Robaczewska, and M. Verlaan, 2002: Inverse 3D shallow water flow modeling of the continental shelf. *Cont. Shelf Res.,* **22,** 465–484.

Høydalsvik, F., and J. E. Weber, 2003: Mass transport velocity on free barotropic Poincaré waves. *J. Phys. Oceanogr.,* **33,** 2000–2012.

Hutula, T., M. Pulkkanen, B. Arkhipov, M. Lepparanta, V. Solbakov, K. Shirasawa, and K. Salonen, 2010: Modeling circulation in an ice-covered lake. *Est. J. Earth Sci.,* **59,** 298–309.

Jay, D. A., and M. J. Bowman, 1975: The physical oceanography and water quality of New York Harbor and western Long Island Sound. State University of New York Marine Sciences Research Center Tech. Rep. 23, 71 pp.

——, and E. P. Flinchem, 1997: Interaction of fluctuating river flow with a barotropic tide: A test of wavelet tidal analysis methods. *J. Geophys. Res.,* **102,** 5705–5720.

——, and T. Kukulka, 2003: Revising the paradigm of tidal analysis—The uses of non-stationary data. *Ocean Dyn.,* **53,** 110–125.

Kagan, B. A., and E. V. Sofina, 2010: Ice-induced seasonal variability of tidal constants in the Arctic Ocean. *Cont. Shelf Res.,* **30,** 643–647.

Knight, R. J., and R. W. Dalrymple, 1976: Winter conditions in a macrotidal environment, Cobequid Bay, Nova Scotia. *Rev. Geogr. Montreal,* **30,** 65–85.

Kukulka, T., and D. A. Jay, 2003: Impacts of Columbia River discharge on salmonid habitat: 1. A nonstationary fluvial tide model. *J. Geophys. Res.,* **108,** 3293, doi:10.1029/2002JC001382.

Langleben, M., 1982: Water drag coefficient of first-year sea ice. *J. Geophys. Res.,* **87** (C1), 573–578.

MacAyeal, D. R., 1984: Thermohaline circulation below the Ross Ice Shelf: A consequence of tidally induced vertical mixing and basal melting. *J. Geophys. Res.,* **89** (C1), 597–606.

Madsen, O., and M. Bruno, 1986: A methodology for the determination of drag coefficients for ice floes. *Proc. Fifth Int. Offshore Mechanics and Arctic Engineering Symp.,* Tokyo, Japan, American Society of Mechanical Engineering, Vol. 4, 410–417.

Maln, J., L. Bengtsson, and A. Terzhevik, 1998: Field study on currents in a shallow ice-covered lake. *Limnol. Oceanogr.,* **43,** 1669–1679.

Mellor, G., and L. Kantha, 1989: An ice-ocean coupled model. *J. Geophys. Res.,* **94** (C8), 10 937–10 954.

Miller, R. L., and J. P. St. John, 2006: Modeling primary production in the lower Hudson River estuary. *The Hudson River Estuary,* J. S. Levington and J. R. Waldman, Eds., Cambridge University Press, 140–153.

Morse, B., B. Burrell, A. St Hilaire, N. Bergeron, D. Messier, and T. T. Quach, 1999: River ice processes in tidal rivers: Research needs. *Proc. Canadian River Ice Workshop,* Winnipeg, Canada, Canadian Committee of River Ice Processes in the Environment, 388–399.

——, B. Ringô, D. Messier, T. Thanh-Quach, and E. Stander, 2006a: Hydrodynamics of a mesotidal estuary in winter. *J. Cold Reg. Eng.,* **20,** 95–115.

——, ——, E. Stander, J.-L. Robert, D. Messier, and T. Thanh-Quach, 2006b: Growth and decay of estuary ice cover. *J. Cold Reg. Eng.,* **20,** 70–94.

Murty, T. S., and G. Holloway, 1985: Influence of marginal ice cover on storm surges. *J. Waterw. Port Coastal Ocean Eng.,* **11,** 329–336.

Nguyen, A. T., D. Menemenlis, and R. Kwok, 2011: Arctic ice-ocean simulation with optimized model parameters: Approach and assessment. *J. Geophys. Res.,* **116,** C04025, doi:10.1029/2010JC006573.

Nitche, F. O., and Coauthors, 2007: Regional patterns and local variations of sediment distribution in the Hudson River estuary. *Estuarine Coastal Shelf Sci.,* **71,** 259–277.

Parker, B. B., 1984: *Frictional Effects of the Tidal Dynamics of a Shallow Estuary*. John Hopkins University, 292 pp.

Parthasarathy, R. N., and M. Muste, 1994: Velocity measurements in asymmetric turbulent channel flows. *J. Hydraul. Eng.,* **120,** 1000–1020.

Pawlowicz, R., B. Beardsley, and S. Lentz, 2002: Classical tidal harmonic analysis including error estimates in MATLAB using T_TIDE. *Comput. Geosci.,* **28,** 929–937.

Pease, C. H., and J. E. Overland, 1984: An atmospherically driven sea-ice drift model for the Bering Sea. *Ann. Glaciol.,* **5,** 111–114.

——, S. A. Salo, and J. E. Overland, 1983: Drag measurements for first-year sea ice over a shallow sea. *J. Geophys. Res.,* **88** (C5), 2853–2862.

Prinsenberg, S. J., 1986: The circulation pattern and current structure of Hudson. *Canadian Island Seas,* E. P. Martini, Ed, Oceanography Series, Vol. 44, Elsevier, 163–186.

——, 1988: Damping and phase advance of the tide in western Hudson Bay by the annual ice cover. *J. Phys. Oceanogr.,* **18,** 1744–1751.

——, and I. K. Peterson, 2002: Variations in air-ice drag coefficient due to ice surface roughness. *Int. J. Offshore Polar Eng.,* **12,** 121–125.

Ralston, D. K., W. R. Geyer, and J. A. Lerczak, 2008: Subtidal salinity and velocity in the Hudson River estuary: Observations and modeling. *J. Phys. Oceanogr.,* **38,** 753–770.

Redfield, A. C., 1950: The analysis of tidal phenomena in narrow embayments. Massachusetts Institute of Technology and Woods Hole Oceanographic Institution Papers in Physical Oceanography and Meteorology Vol. 11 (4), 36 pp.

——, 1980: *The Tides of the Waters of New England and New York*. Woods Hole Oceanographic Institution, 108 pp.

Saucier, F. J., S. Senneville, S. J. Prinsenberg, F. Roy, G. Smith, P. Gachon, D. Caya, and R. Laprise, 2004: Modeling the sea ice-ocean seasonal cycle in Hudson Bay, Foxe Basin and Hudson Strait, Canada. *Climate Dyn.,* **23,** 303–326.

Savant, G., G. L. Brown, and C. Berger, 2009: Friction in ice covered flows. *Proc. 33rd IAHR Congress: Water Engineering for a Sustainable Environment,* Vancouver, Canada, International Association of Hydraulic Engineering & Research, 1300–1307.

Scully, M. E., W. R. Geyer, and J. A. Lerczak, 2009: The influence of lateral advection on the residual estuarine circulation: A numerical modeling study of the Hudson River estuary. *J. Phys. Oceanogr.,* **39,** 107–124.

Sergienko, O. V., and C. L. Hulbe, 2011: 'Sticky spots' and subglacial lakes under ice streams of the Siple Coast, Antarctica. *Ann. Glaciol.,* **52,** 18–22.

Smithson, M. J., A. V. Robinson, and R. A. Flather, 1996: Ocean tides under the Filchner-Ronne Ice Shelf, Antarctica. *Ann. Glaciol.,* **23,** 217–225.

St-Laurent, P., F. J. Saucier, and J.-F. Dumais, 2008. On the modification of tides in a seasonally ice-covered sea. *J. Geophys. Res.,* **113,** C11014, doi:10.1029/2007JC004614.

Sverdrup, H. U., 1926: *Dynamics of Tides on the North-Siberian Shelf: Results from the Maud Expedition*. Vol. 6, Geofysiske Publikasjoner, Grondahl, 75 pp.

Swanson, R. L., 1976: Tides. *Marine Ecosystems Analysis (MESA) Program, New York Bight Atlas Monogr.,* No. 4., New York Sea Grant Institute, 31 pp.

Thoma, M., K. Grosfeld, C. Mayer, and F. Pattyn, 2010: Interaction between ice sheet dynamics and subglacial lake circulation: A coupled modelling approach. *Cryosphere,* **4,** 1–12.

USACE, 1997: Hydrologic engineering requirements for reservoirs. United States Army Corps of Engineers Engineering and Design Manual EM 1110-2-1420, 115 pp.

——, 2006: Ice engineering. United States Army Corps of Engineers Engineering and Design Manual EM 1110-2-1612, 475 pp.

USGS, 1982: Measurement and computation of streamflow: Volume 2. Computation of discharge. U.S. Geological Survey Water-Supply Paper 2175, 373 pp.

Volkov, V. A., O. M. Johannessen, V. E. Borodashev, G. N. Voinov, L. H. Pettersson, L. P. Bobylev, and A. V. Kouraev, 2002: Tides and tidal streams. *Polar Seas Oceanography: An Integrated Case Study of the Kara Sea,* V. A. Volkov, Ed., Springer-Verlag, 147–216.

Wang, J., H. Haoguo, D. Schwab, G. Leshkevich, D. Beletsky, N. Hawley, and A. Clites, 2010: Development of the Great Lakes Ice-Circulation Model (GLIM): Application to Lake Erie in 2003-2004. *J. Great Lakes Res.,* **36,** 425–436.

Warner, J. C., W. R. Geyer, and L. A. Lerczak, 2005: Numerical modeling of an estuary: A comprehensive skill assessment. *J. Geophys. Res.,* **110,** C05001, doi:10.1029/2004JC002691.

WMO, 2010: Manual on stream gauging: Volume II—Computation of discharge. World Meteorological Organization Rep. 1044, 198 pp.